Modeling and experimental studies of coating delamination of biodegradable magnesium alloy cardiovascular stents

Chenxin Chen,[†‡※] Jinyun Tan,[⊥※] Wei Wu,[*‡§] Lorenza Petrini,[^] Lei Zhang,[†] Yongjuan Shi,[†] Emanuele Cattarinuzzi,[‡] Jia Pei,[†] Hua Huang,[†] Wenjiang Ding,[†] Guangyin Yuan,[*†] Francesco Migliavacca,[*‡]

[†]*National Engineering Research Center of Light Alloy Net Forming & State Key Laboratory of Metal Matrix Composite, Shanghai Jiao Tong University, Shanghai, 200240, China*

[‡]*Laboratory of Biological Structure Mechanics (LaBS), Department of Chemistry, Materials and Chemical Engineering "Giulio Natta", Politecnico di Milano, Milan, Italy*

[⊥]*Department of Vascular Surgery, Huashan Hospital of Fudan University, No.12 Mid-Wulumuqi Rd, Shanghai, China, 200040*

[§]*Department of Mechanical Engineering, The University of Texas at San Antonio, One UTSA Circle San Antonio, TX 78249-0669*

^ *Department of Civil and Environmental Engineering, Politecnico di Milano, Italy.*

[※]*these authors contributed equally to this work.*

* *Corresponding author. E-mail: wei.wu2@utsa.edu.*

* *Corresponding author. E-mail: gyyuan@sjtu.edu.cn.*

* *Corresponding author. E-mail: francesco.migliavacca@polimi.*

This is a pre-peer-review version of an article published in ACS Biomaterials Science & Engineering 4(11): 3864-3873. The final authenticated version is available online at: https://pubs.acs.org/doi/10.1021/acsbiomaterials.8b00700.

ABSTRACT

Biodegradable magnesium alloy stents exhibit deficient corrosion period for clinic applications, making the protective polymer coating more crucial than drug-eluting stents with the permanent metal scaffold. We implemented a cohesive method based on finite element analysis method to predict the integrity of adhesive between coating and stent during the crimping and deployment. For the first time, the three-dimensional quantitative modeling clarified the conditions for polymer coating delamination and stress concentration. The fracture and micro-creaks of coatings were confirmed by scanning electron microscopy observation. Moreover, we analyzed four possible factors, i.e., strut material, stent design, coating polymer and thickness of the coating, affecting the stent-coating damage and the distribution of the stress. The cohesive modeling provides a greater understanding of stent-coating damage and shows how computational analyses can be implemented in the design of coated biodegradable magnesium stents.

KEYWORDS: Polymer coating; biodegradable magnesium alloy stent; delamination; cohesive zone method; finite element analysis

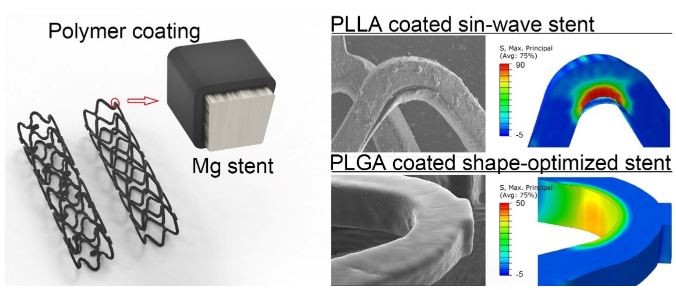

INTRODUCTION

In recent years, drug-eluting stents have become the standard therapy for percutaneous coronary intervention (PCI), to cure the treatment of coronary artery stenosis[1-2]. Bioabsorbable polymer-based vascular scaffolds (BVS) and biodegradable magnesium alloy stents (BMS) were developed to overcome the shortcomings of drug-eluting stents, leaving no permanent implant with short-term support and long-term degradation to restore vessel function, avoiding a series of disadvantages[3]. However, a series of clinical results of BVS show that the bioabsorbable polymer-based scaffold has noninferior rates of target lesion failure at 1 year to DES, but with a higher incidence of device thrombosis than the metallic stent through 2-year and 3-year clinical follow-ups[4-6]. Considering the differentiating failure modes in metallic and polymeric devices, BVS not only degrade but also possess significant localized structural irregularities that cause asymmetric degradation, which could be an explanation for the clinical results[7].

Compared to the bioabsorbable aliphatic polymers of BVS, such as poly(l-lactic acid) (PLLA) and poly(lactic-co-glycolic acid) (PLGA), some of the biodegradable magnesium alloys have superior mechanical properties and uniform degradation process[8-10], which might lead to better long-term clinic behavior than BVS. However, the degradation rates of Mg alloys are still too high at the initial stage of implantation for the clinical requirements[11-12]. On the one hand, applying polymer coatings on Mg alloys could reduce the degradation rate of Mg and carry anti-proliferative drugs to avoid initial stenosis[13-16]. In the light of observed coating damages on DES [17-18], the integrity and cohesion of polymer coating on BMS are more important, as the delamination or fracture of the coating would expose the Mg alloy strut surface and accelerate the localized corrosion rate, which might lead to vascular restenosis and prevent vessel endothelialization[18-20].

Finite element analysis (FEA) has been widely used to guide stent design and simulate the deformation and degradation of the implanted device[21-25]. Cohesive zone method (CZM) based on a peeling model could efficiently reflect the adhesive property between two surfaces[26-27], for example stent and coating. A series of 2D CZM simulation and experiments have been conducted for stainless drug-eluting stent, in order to predict and explicate a variety coating-damages, including delamination, webbing, and buckling[28-30]. The CZM has also been applied to design and analyze coated biodegradable magnesium stent[25, 31]. Nevertheless, the previous simulations of the adhesion of polymer coatings and metallic stents are based on two-dimensional models. The specific deformation of coating in the thickness direction of stent and the effects of stent-balloon contact cannot be evaluated in such a model.

The present study aims to develop a 3-D model to simulate the deformation process and stress distribution of polymer coatings, meanwhile predicting and evaluating the coatings integrity and delamination tendency. This work is carried out considering two Mg alloys: commercial Mg alloy AZ31 and Mg-Nd-Zn-Zr (abbr. JDBM), a magnesium alloy made by with excellent mechanical properties, and uniform degradation behavior[32]. High-quality micro-tubes[33], stents[34] and polymer coatings[15-16] used in this work are progressed by the authors. The 3D FEA modeling for polymer-coated magnesium stent using CZM is put forward first to date.

MATERIALS AND METHODS

Stent samples and Materials properties

The chemical composition and processing of two magnesium alloy tubes, AZ31 and JDBM, can be found in our previous work[33]. Two designs, the stent with sine-wave ring (abbr. SIN) and shape-optimized stent (abbr. OPT) designed by our group, were shown in Fig.1. The repeated units were captured form each design shown in colored, to build the FEA model. The outer diameter and thickness of stents were 3.00mm and 160μm respectively.

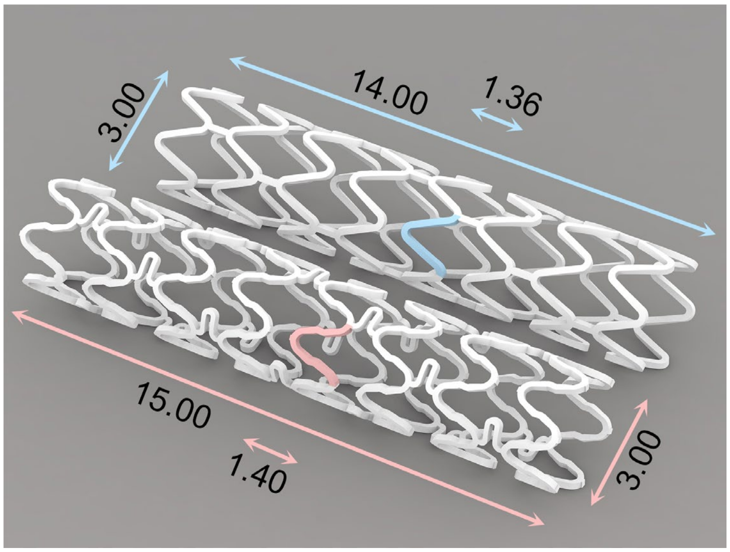

Fig. 1 Geometries of SIN (top) and OPT stent (bottom) with the basic dimensions. One strut of each design (in red and blue highlight) was chosen for the modeling.

The AZ31 tubes were cut into SIN stents (abbr. AZ31-SIN), while the JDBM tubes were cut into OPT stents (abbr. JDBM-OPT). To adjust the unsmooth surface caused by the laser cutting, the stents were polished with the electrochemical method and were then washed via ultra-phonic ethanol cleaning before drying[33]. After fluoride treatment of both AZ31-SIN and JDBM-OPT stents, the stents were prepared using an ultrasonic spray-coating technology as described in our previous work[16]. Poly(l-lactic acid) (abbr. PLLA) and poly(lactic-co-glycolic acid) (abbr. PLGA) were used for stent coating spray. PLGA is in mole ratio of LA/GA=50/50. PLLA and PLGA with an weight-average molecular weight of ~100,000 g/mol were bought from Jinan Daigang Biomaterial Co., Ltd. (Shandong, China). No drug is contained in those polymer coatings.

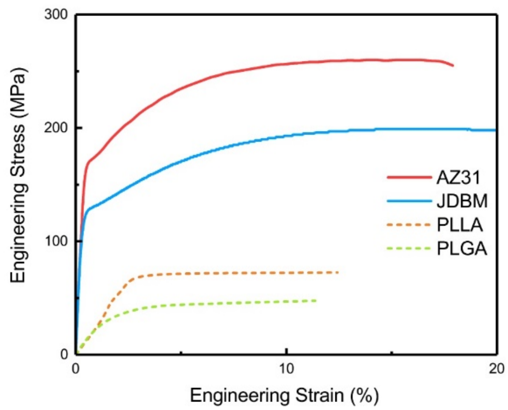

Fig. 2 The stress-strain curves of AZ31 and JDBM stent materials, and PLLA and PLGA coatings.

In our FEA model, JDBM and AZ31 alloy were used as stent platform materials, while PLLA and PLGA were used for the coating materials. The stress-strain curves of JDBM and AZ31 were obtained from tensile mechanical tests of micro-tubes[33]. The polymers mechanical properties were taken from the study by Paryab et al.[35]. The stress-strain curves are shown in Fig.2. The modulus of elasticity and Poisson's ratio of magnesium alloys are 43.5GPa and 0.35, respectively; the yield strength of JDBM and AZ31 are 120MPa and 175MPa, respectively (Table.1).

Table.1 Materials property in the FEA

Parameters	Stent		Coating	
	AZ31	JDBM	PLLA	PLGA
Density, ρ $(\mathrm{kg} \cdot m^{-3})$	1.78	1.84	1.30	1.30
Young's modules, E (GPa)	43.5	43.5	2.71	1.58
Poisson's ratio, ν	0.35	0.35	0.3	0.3
Yield stress, σ (MPa)	175	122	67.9	29.7

Cohesive zone method (CZM)

The CZM approximation describes separation phenomenon caused by crack initiation and propagation between two surfaces. In this approach, the initial creak in interface was valued by a traction-separation law, which is based on energy principles[26]. In FEA application, a single layer of cohesive elements (usually with a thickness of zero) is built between two surfaces as a “bonding” segment[36]. During the simulation, the cohesive elements resist the tensile loads, separating the adjoining surfaces until the initiation of damage and the potential failure of the elements.

A bilinear traction–separation law is applied in the CZM in this study. The pure model constitutive law of traction–separation responses in the normal direction and tangential direction is illustrated in Fig. 3. This model assumes a linear elastic behavior before damage in the interface. Once an initiation criterion σ_n/σ_t is reached, the damage is initiated. Under continuous loading, damage spreads until the final fracture occurs.

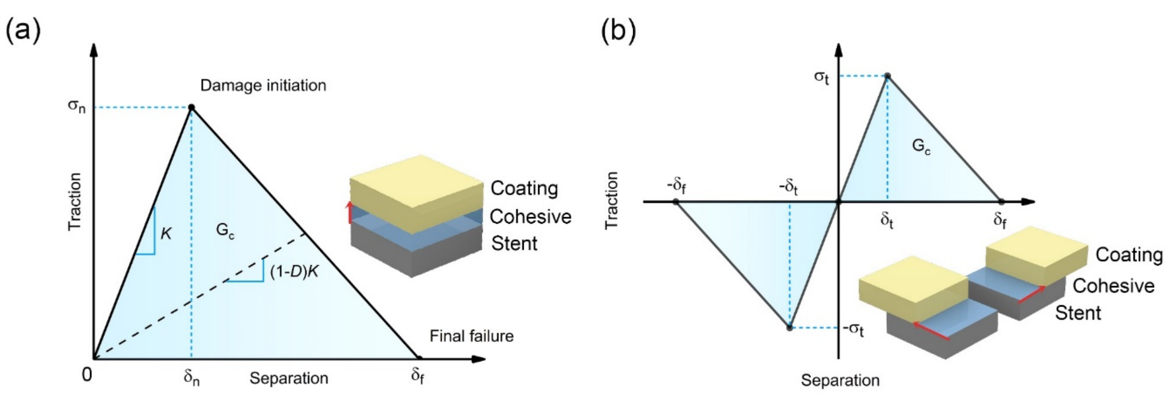

Fig. 3 Schematic of the bilinear traction-separation law used for the cohesive elements, in the normal (a) and (b) in the tangential direction. Yellow and gray cubes stand for coating and stent elements, respectively. Red arrows show the traction direction.

The traction–separation constitutive relationship can be expressed as

$$\sigma = \begin{cases} K\delta, & \delta \leq \delta_n \\ (1-D)K\delta, & \delta_n \leq \delta \leq \delta_f \\ 0, & \delta \geq \delta_f \end{cases} \tag{1}$$

and

$$D = \begin{cases} 0, & \delta \leq \delta_n \\ \dfrac{\delta_f(\delta-\delta_0)}{\delta(\delta_f-\delta_0)}, & \delta_n \leq \delta \leq \delta_f \\ 1, & \delta \geq \delta_f \end{cases} \tag{2}$$

where σ and δ are the stress and displacement of separation. δ_n and δ_f are the initial damage displacement and fracture displacement. *D* is a damage variable, overall scalar stiffness degradation, ranging from 0 to 1. *K* is the initial interfacial stiffness, which is treated as a penalty parameter and does not represent a physically measurable quantity[27].

The critical energy release rate G_c can be calculated by

$$G_c = \frac{1}{2}\sigma_n\delta_f \tag{3}$$

where σ_n is the interfacial critical stress.

In Eqs.(1)–(3), we assume that $\sigma_n = \sigma_t$, and $\delta_n = \delta_t$, so that the stresses, displacements, and critical fracture energy can be represented for the components in normal and tangential directions. In this simulation, the adhesion data is captured in an enhanced 90^{o} peeling test, which is reported in our previous work by a penalty function method[27, 37]. Peeling test with simultaneous imaging of the samples has been carried out by means of an in-house developed micro-tensile equipment[38].

Finite element model

Considering the symmetry of the stent, one-sixth ring was developed for both SIN stent and OPT stent. Moreover, the influence of the balloon-stent interaction on coating delamination was investigated.

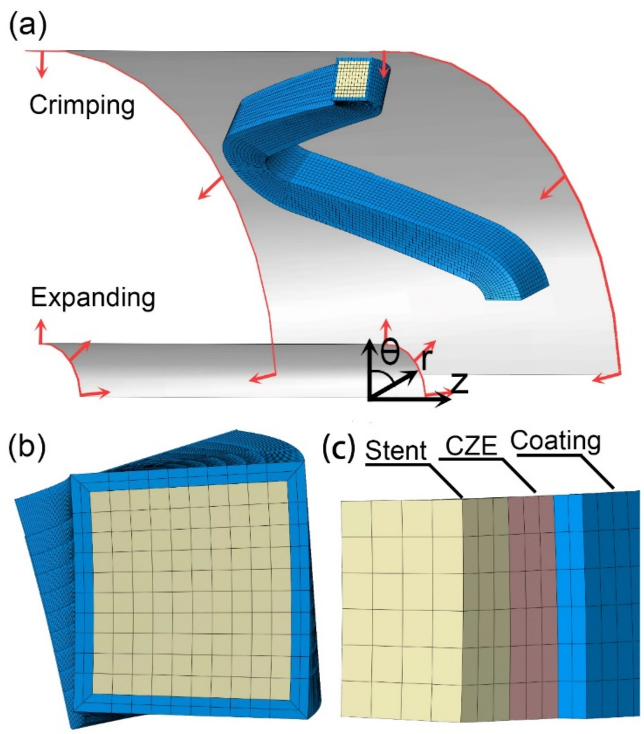

Fig. 4 The FEA model of stent unit and two driving cylindrical surfaces (a), with boundary conditions in circumferential direction and displacement loading in radial direction. The cross-section of the model (b) includes stent (blue) and coating (yellow) meshes, and cohesive zone element (red) between with zero thickness (c).

A theta-symmetry (Fig.4a) was applied to the nodes of the two distal surfaces of the structure and a radial displacement is applied to the balloon. The coating was modeled with a series thickness of 5μm, 10μm and 15μm covering the stents. Between the stent and the coating, and at the edge of coating, there is a monolayer of cohesive elements of zero thickness, as shown in Fig.4c. The balloon was modeled with a cylindrical surface. A general contact algorithm was applied to simulate interaction between coating and stent interaction, between abluminal side of coating and crimping device, and between luminal side of the coating and the balloon, setting a normal hard contact and a tangential behavior with a coefficient of friction of 0.2. In this way the crimping and expansion deformation of stent are driven by the inner and outer shells (Table 2).

Table.2 Boundary conditions for stent-coating deformation

Time,	Outer surface (crimping)		Inner Surface (expansion)	
s	Diameter, mm	Contact state	Diameter, mm	Contact state
0	3.1	☑	-	☐
0.5	3.0	☑	-	☐
1.5	1.3	☑	1.1	☑
2.0	-	☐	1.1	☑
3.5	-	☐	3.1	☑
4.0	-	☐	-	☐

The coating and stent were meshed with eight-node brick elements with reduced integration (C3D8R), 10 and 2 layers in stent and coating thickness direction respectively. The cohesive layer was meshed with eight node tridimensional cohesive elements (COH3D8) with average max edge length of 15μm. And the balloon was meshed using four nodes surface elements with reduced integration (SFM3DR). The simulations were run using the ABAQUS/Explicit code 6.14 (Dassault Systèmes, Vélizy-Villacoublay, France).

SEM characterization

The surface morphology of the PLLA and PLGA coatings were examined by scanning electron microscopy (SEM, JSM 7600F, Japan). Before SEM observation, samples were coated with a layer of gold with a thickness of ~20 nm by a sputter coater (SHINKKU VD MSP-1S, Japan).

Objective of the study

Firstly, three FEA scenarios were simulated and validated by experiments: the AZ31-SIN stent coated with PLLA and PLGA, respectively, and the JDBM-OPT stent coated with PLGA. Only two stent platforms were provided due to the difficulty in manufacturing stent samples. The thickness of coatings is 10μm, which is calculated by the mass increment after ultrasonic spray-coating. In this section, the critical energy release rate G_c of 58.2 J/m^2 is captured by peeling test mentioned previous.

Secondly, for one stent, namely PLLA coated AZ31-SIN stent, the process of delamination was further investigated. The traction of cohesive element layer during crimping and expansion were plotted and divided in the local coordinate system. The sequence of damaging and deleting of cohesive element during the process of coating debonding would be evaluated.

Thirdly, as different coating material properties and stent material influence the adhesion interface states and deformations of the coatings, the influence of stent design and material on coating deformation behavior was investigated. For the 3D models, we build up three different stent platforms: AZ31-SIN stent, JDBM-SIN stent and JDBM-OPT stent, coated with PLLA with 10μm thickness. In order to present the various behavior of coating deformation on a different platform, another smaller interface fracture energy G_c of 43.5 J/m^2 was assumed.

Furthermore, to investigate influence of coating materials and thickness on coating peeling, two materials (PLLA and PLGA) and three coating thicknesses (5, 10 and 15μm) are combined with the three stent platforms (AZ31-SIN, JDBM-SIN and JDBM-OPT) for 18 simulation scenarios. The range of coating thickness is based on the current commercial stent coating thicknesses, and can provide a reference for future coating process optimization. For each scenario, a critical interface fracture energy G_c' was calculated to avoid coating delamination during the expansion step and compared to other scenarios.

RESULTS

Simulation predicting and experiment validation

Three FEA scenarios were simulated and validated by experiments, as shown in Fig.5. The first row is the SIN stent coated with PLLA (a-c), the second row is the same stent coated with PLGA (d-f) and the last row is the OPT stent coated with PLGA (g-i).

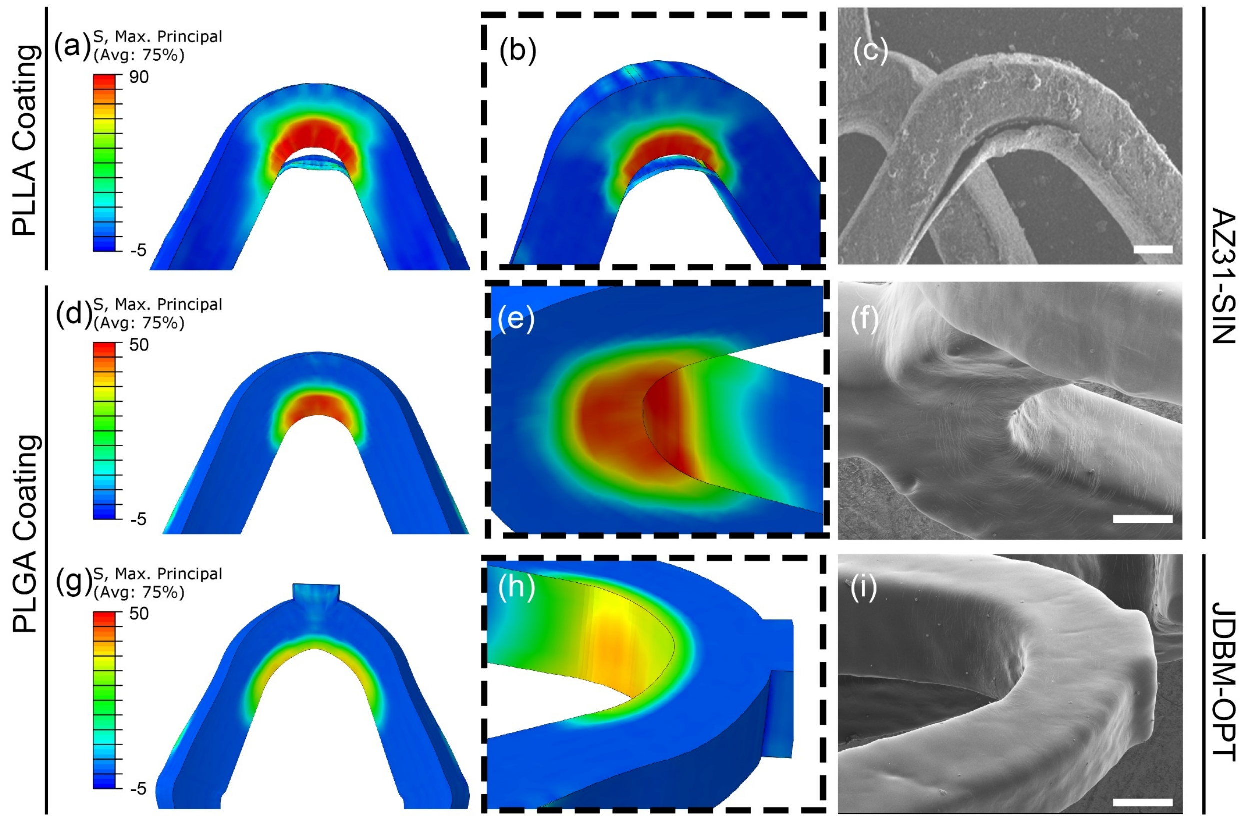

Fig. 5 The maximum principal stress distributions on the polymer coatings and the SEM images for coating delamination (Scale bar represents 100 μm). The delamination of PLLA coating on the AZ31-SIN stent (a and b) is consistent with the SEM image (c). The PLGA coatings maintained their integrity on JDBM-SIN stent (d) and JDBM-OPT stent (g); while the coating on SIN stent has higher stresses (e) and microcracks (f) with respect to the OPT stent (h and i).

The distributions of the maximum principal stress of the PLLA coating are shown in two different perspectives (Fig. 5a-b). The predicted fractures and delamination of PLLA coatings in SIN stent were similar to the experiment (Fig. 5c). As shown in Fig. 5d, the PLGA coating in the SIN stent should remain integrated after the expansion, which was also confirmed by SEM observations (Fig. 5f). Furthermore, the simulation found coating stress concentration near the inside edge of the stent bow (Fig. 5d and e). In the SEM observation, dense micro-cracks exhibit a similar pattern to the contour of the stress distribution in the same region (Fig. 5f). The density of the micro-cracks looked consistent with the distribution of maximum principal stress on the coating surface.

The comparison between the PLGA coatings in SIN and OPT stent (Fig. 5d & e) shows that the coating in the OPT stent has a much lower peak stress than that in the SIN stent (33MPa vs 49MPa), and no micro-cracks can be observed in SEM image (Fig. 5i).

Stress fluctuation during crimping and expansion

The deformation and maximum principal stress distribution of PLLA coating in SIN stent after crimping and expansion are shown in Fig. 6. Although the coating remained intact after crimping (Fig. 6a), it had delamination inside strut bow, and fractured at the inside edge of the coating after the expansion (Fig. 6b).

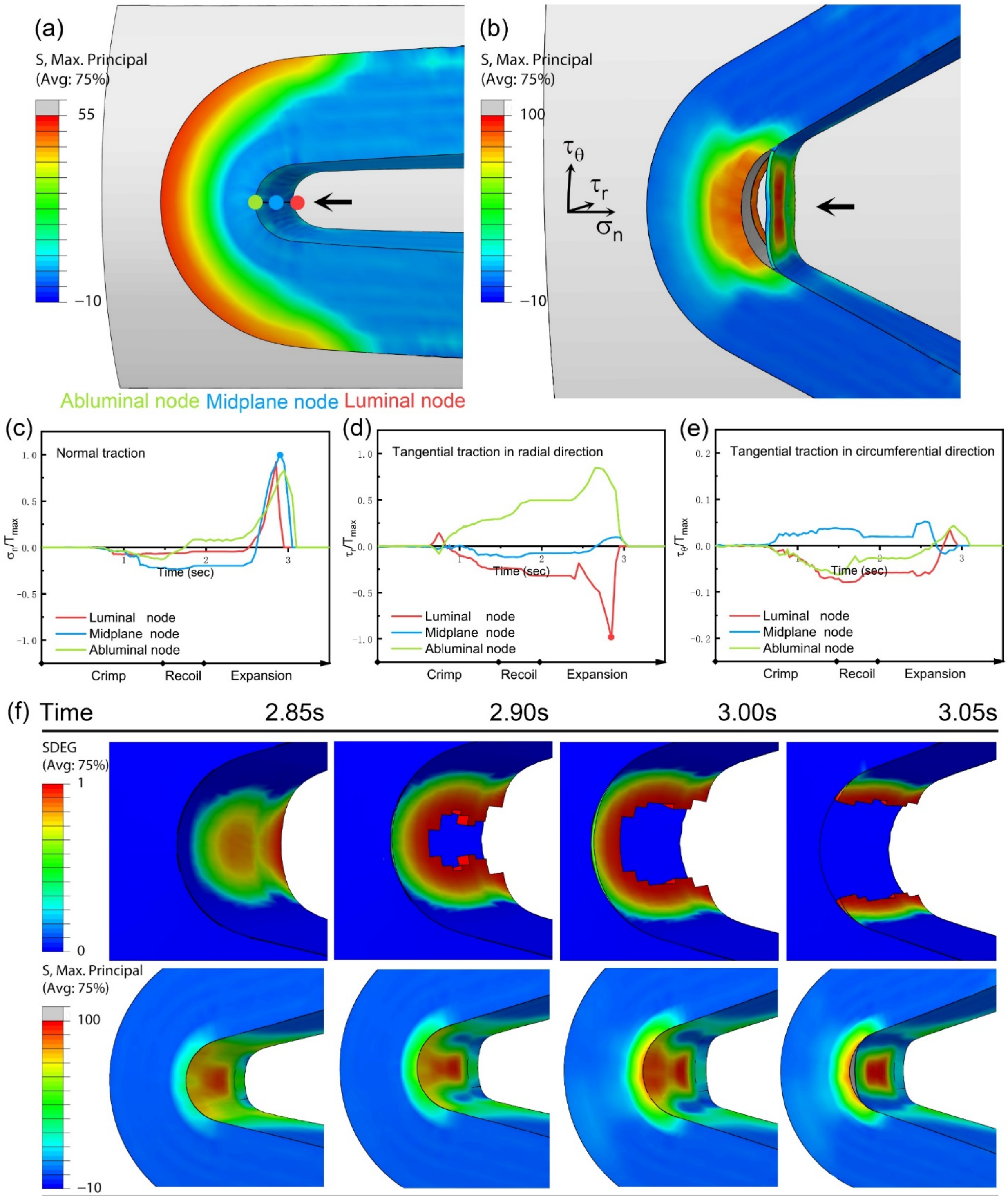

Fig. 6 The maximum principal stress distributions of polymer coating after crimping (a) and after expansion (b)..

Three collinear dots show the locations of representative nodes of the cohesive layer, indicated by the black arrow (a). The coating delamination is indicated by the black arrow (b). The normal traction (σ_n), tangential traction in radial direction (τ_r) and in circumferential direction (τ_θ) for the three nodes are shown in (c), (d) and (e), respectively. The sequence of stiffness degradation distribution (SDEG) of the cohesive elements and maximum principal stress distribution of the coating elements during the initial period of the delamination are shown in (f).

Three collinear nodes were selected from cohesive layer at luminal (red), midplane (blue) and abluminal (green) location to analyze the stress in the cohesive layer. According to the local coordinate system defined in Fig. 5b (n, r and θ in normal, radial and circumferential direction), the tractions of these nodes in the three directions are shown in Fig. 5c, d, and e, respectively. The normal traction σ_n of the three nodes were in compressive state during crimping and recoil. During expansion σ_n of these nodes changed to a tensile state and increased rapidly, and the midplane node reached the T_{max} at 2.80s, then the corresponding CZE was damaged and deleted in sequence. The peak σ_n of the luminal and the abluminal node reached are $0.96T_{max}$ and $0.82T_{max}$, respectively. These result shows that the normal traction is not the only reason for the coating delamination at the luminal and abluminal locations. As for the tangential traction in the radial direction (τ_r), the midplane node reached a peak value of $0.14T_{max}$ during the expansion (Fig. 6d). However, τ_r of the luminal node reached $-T_{max}$ at 2.85s almost at the same time it reached the peak value of σ_n. Then, the corresponding CZE were damaged and coating delamination happened at the luminal location. The tangential traction τ_r of the abluminal node reached $0.84T_{max}$ at 2.65s, ealier than the normal traction got the peak value. In the circumference direction, the tangential tractions (τ_θ) for the three nodes fluctuated around zero because of the geometrical symmetry (Fig. 6e).

The sequence of stiffness degradation distribution of cohesive elements and maximum principal stress distribution of the coating elements during the initial period of the delamination revealed the detailed process of cohesive elements degradation (Fig. 6f). The midplane node and luminal node got damaged at 2.85s, but the cohesive layer was still intact. The initial debond of coating appeared in the luminal and middle zone at 2.90s. Subsequently, the debond of coating spread around and the concentration of stress occurred around the abluminal node at 3.00s. Next timeframe, all of the cohesive elements on the symmetric line were deleted and the delamination of coating took place at 3.05s.

The influence of stent design and material on coating deformation

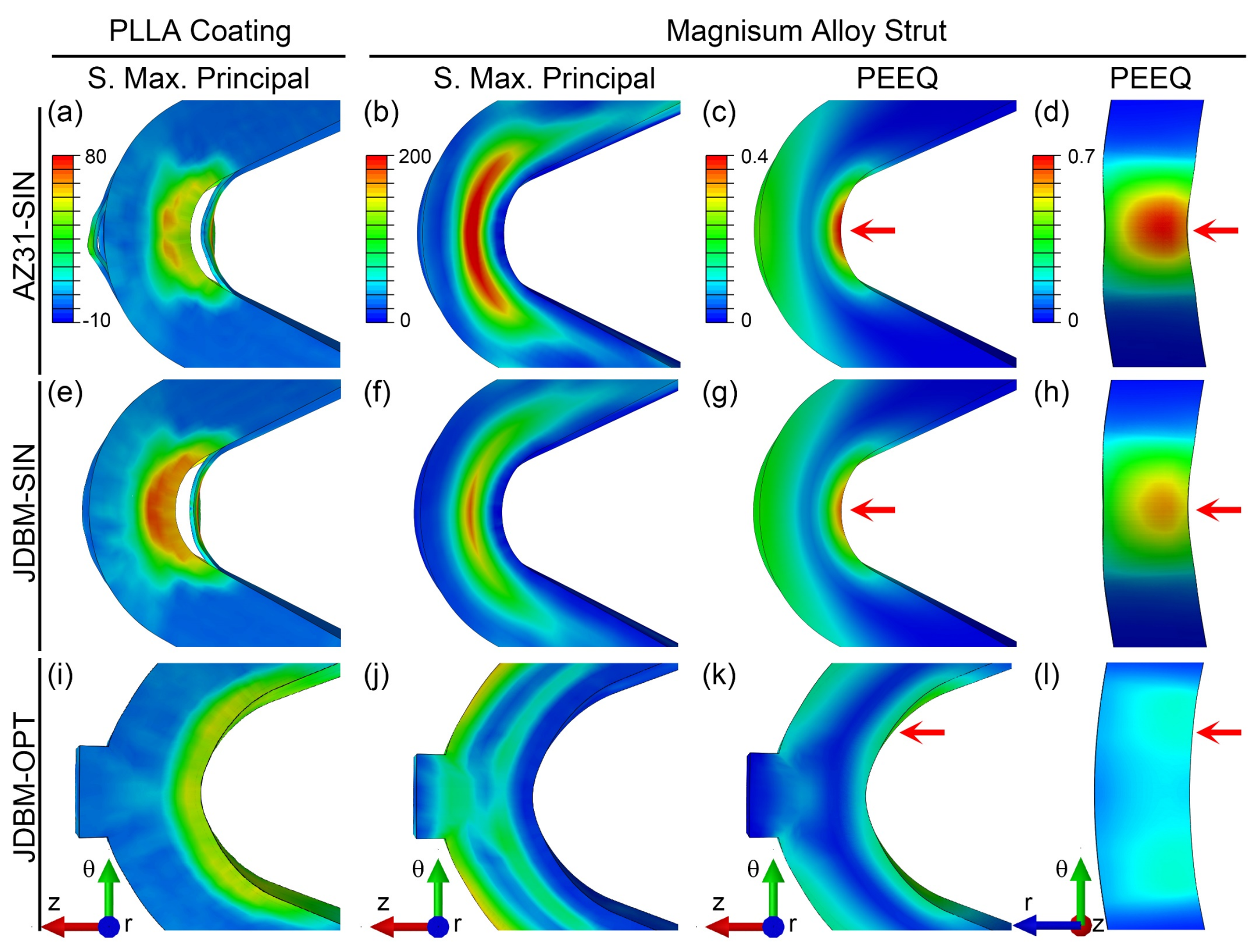

Fig. 7 The maximum principal stress distributions of PLLA coatings with a thickness of 10 μm on the AZ31-SIN

stent (a), JDBM-SIN stent (e) and JDBM-OPT stent (i) expanded to the inner diameter of 3.1mm and recoiled, with an interface fracture energy G_c of 43.5 J/m^2. The max principal stress in the stents are shown in panels b, f and j. The equivalent plastic strain (PEEQ) distributions of the abluminal strut surface are shown in panels c, g and k, and for the lateral strut surface in panels d, h and l. Two legends are used to highlight the difference in abluminal and lateral surface; the locations of maximum PEEQ are marked by three red arrows.

As for the influence of the stent material and design on the coating deformation, the first column of Fig. 7 shows the surface morphology and stress distribution of the PLLA coating after crimping and expansion of the three different stent platforms (AZ31-SIN stent, JDBM-SIN stent and JDBM-OPT stent). The PLLA coating on the AZ31-SIN stent delaminated at both inside and outside edge of the bow after being deployed (Fig. 7a). When the material is changed from AZ31 alloy to JDBM, the coating on JDBM-SIN sent delaminated at the inside edge while the outside edge of coating remained intact (Fig.7e). On the other hand, when the stent material is JDBM but the stent design is changed to OPT, all the PLLA coating on JDBM-OPT stent remains intact after balloon expansion and recoil (Fig. 7i). The peak value of maximum principal stress of coatings decreased from 76.2MPa to 56.73MPa (Fig.7e & i).

To further disclose the influence of stent material and design, the struts of AZ31-SIN, JDBM-SIN and JDBM-OPT stent were isolated to compare the distribution of maximum principal stress (S. Max. Principal) and equivalent plastic strain (PEEQ) (Fig. 7b, c, f, g) in the stent after expansion and recoil. The same design and the same elastic modulus of alloys generated similar patterns of stress and strain for AZ31-SIN and JDBM-SIN stent. The peak values of max principal stress of AZ31-SIN and JDBM-SIN stent are 245.3MPa and 203.6MPa, respectively. And the corresponding peak value of equivalent plastic strain are 0.779 and 0.633, respectively. Meanwhile, the locations of peak stress are located at the center part of the strut corner and the locations of peak plastic strain are located at the symmetric line of lateral surface (Fig.7d & 7h). When the stent design is considered, the maximum value of the maximum principal stress of JDBM-OPT stent was decreased to 193.4MPa (Fig.7j), and the PEEQ was significantly reduced to 0.232 (Fig.7k), compared to the JDBM-SIN stent. Meanwhile, the stress concentration was separated into two symmetrical parts and the location of peak value moved away from the center (Fig. 7l).

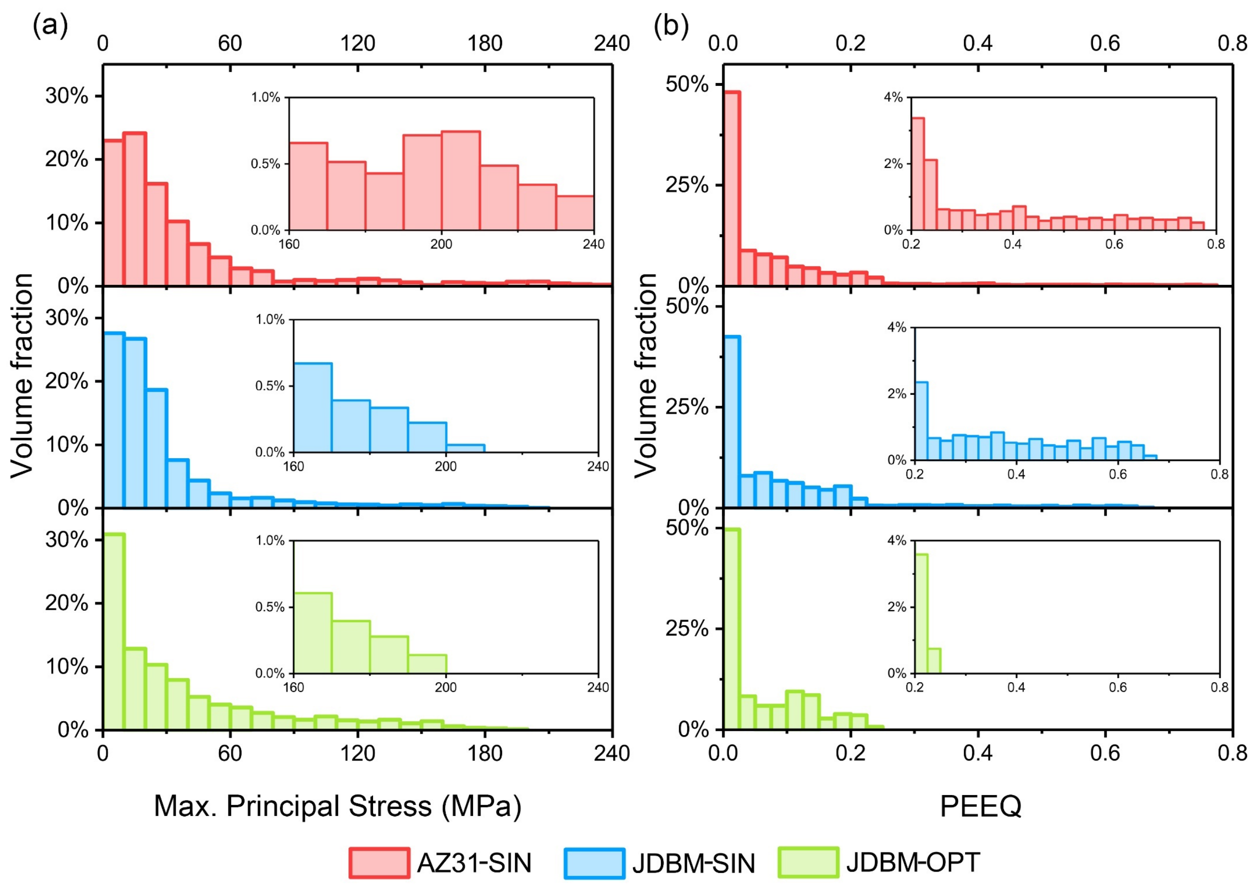

Fig. 8 The volume fraction of maximum principal stress (a), and PEEQ (b) in AZ31-SIN stent (red), JDBM-SIN stent (blue) and JDBM-OPT stent (green).

Considering that the value of the single integration point cannot reveal the deformation behavior comprehensively, the statistics of the volume fraction of stent elements stress are shown in Fig.8. The volume percentage of high stress (≥160MPa), of AZ31-SIN stent, JDBM-SIN stent and JDBM-OPT are 4.14%, 1.71% and 1.42% respectively (Fig. 8a) and the percentage of high plastic deformation (≥0.2), of them are 14.2%, 12.3% and 4.36% respectively (Fig. 8b). These statistics disclose that the AZ31-SIN stent exhibits more severe stress concentration behavior than JDBM-SIN stent. The JDBM-OPT stent decreased the stress concentration fundamentally than JDBM-SIN stent. Stent design plays a crucial factor in the deformation behavior of stent and coating.

The influence of coating materials and thickness

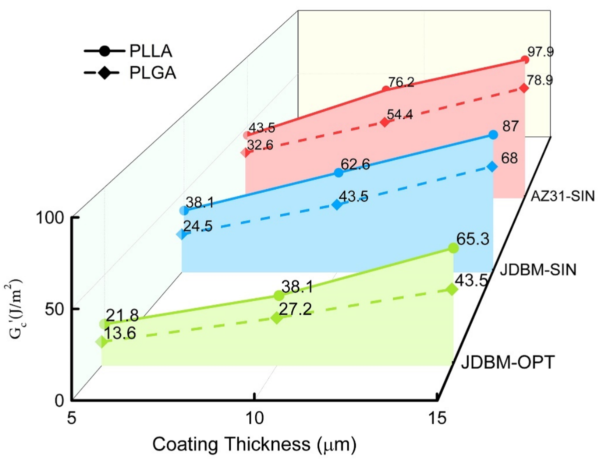

Fig.9 The critical interface fracture energy *Gc'* required to avoid delamination for the combination of different polymer coatings, coating thickness and stent types.

The critical interface fracture energy $G_c{}'$ of each combination of coating materials, thicknesses and stent platforms was evaluated by multiple tentative simulations (Fig. 9). Among them, the JDBM-OPT stent coated with PLGA of the thickness of 5um required an interface fracture energy $G_c{}'$ that is not less than 13.6J/m^2. Therefore the coating remains intact during the deformation. With the increase of coating thickness, the critical interface strength increased accordingly and the critical interface strength required for the PLGA coating of a thickness of 10 and 15um increased to 27.2 J/mm^2 and 43.5 J/mm^2, respectively. Because the PLLA coating has higher elastic modulus and yield strength than those of the PLGA coating (2.71MPa vs. 1.58MPa; 67MPa vs. 29MPa), the critical interface fracture energy of PLLA is higher than that of PLGA, based on the same stent platform. In addition, when the stent material and design are considered, the analysis of the critical interface fracture energy G_c' is consistent with the previous comparison of the stress distribution statistics (Fig. 8). Although both the design and the material of the stent affect the critical interface fracture energy, the primary factor is the design and the influence of the stent material is subordinate relatively. For example, the critical interface fracture energies of PLLA with a thickness of 15um on these stent platforms are 65.3 J/mm^2, 87 J/mm^2 and 97.9 J/mm^2 respectively (Fig. 9). The critical interface fracture increased by 33.2% due to the replacement of the stent design while substituting the AZ31 for JDBM, the critical interface fracture only increased by 12.3%.

DISCUSSION

The study of stent coating delamination is important because the delamination damages the coating integrity and then influences the drug delivery adversely[18, 20, 39]. Furthermore, the coating delamination of biodegradable magnesium alloy stents can accelerate the localized corrosion of the stent platform. This study applied 3D finite element model to predict the coating delamination for three scenarios, and the results are well compatible to experimental tests (Fig. 5). Considering that the FEA framework includes a series of parameters, such as the material properties of the stent and coating, the thickness of the coating and the interface fracture energy G_c, the validated simulation proved the robustness, accuracy and compatibility of the proposed CZM framework. As far as the authors know, this is the first work using 3D model to evaluate the coating delamination of cardivascular stents.

Owing to the symmetry of the boundary conditions in the FEA model, the gap located in the inside edge of the corner shown in the FEA result (Fig. 5b) is smaller than that in the SEM image (Fig. 5c). The inaccuracy introduced by laser-cutting and coating spray, as well as the asymmetric deformation of crimping and expansion, leading to the longer delamination gaps compared to the simulation result.

Compared to the adhesion properties between chronflex AL and 316L stainless steel captured via peeling test by C. Hopkins et al[29], our interface fracture energy G_c is much higher (58.2 J/m^2 vs 29.6 J/m^2 for dry sample). The primary cause is that the fluoride acid corrades the sample surface. The roughness of fluoride magnesium is higher than polished stainless steel, which leads to higher interface fracture energy G_c[13].

The 3D model revealed more information about coating delamination which 2D model cannot find, because 3D model includes the stent thickness, and stent-balloon contact and friction. As shown in Fig. 6, coating delaminated from the inside edge of strut bow and fractured at the inside edge of coating after expansion. This phenomenon is concurrent with the 2D results[28, 30-31]. The 3D result shows that the normal tractions at luminal and abluminal location are not the only reason for the coating delamination there. The sequence of stiffness degradation distribution of cohesive elements during the initial period of the delamination provided the detailed cohesive elements damaging process (Fig. 6f). The contact between coating and balloon plays an important factor on the tangential tractions in the initial phase of delamination. Furthermore, these sequences reveal that the debonding is not instantaneously, but is an incremental process that starts from luminal node towards the abluminal node. This inference is ignored in 2D analysis. It is worth noting that the radial direction is perpendicular to 2D models, which means that the τ_r will be assumed to zero in 2D simulation.

Our analyses showed the influence of the material and the design of the stent platform on coating delamination. Due to the higher yield point of AZ31 compared to JDBM (175MPa vs. 122MPa), the plastic strain accumulative zone of the AZ31-SIN stent spreads to the adjacent area slower than JDBM stent, resulting in a smaller plastic deformation zone with a higher plastic deformation peak (Fig. 7d, h and 8b). Because of the concentrated severe plastic deformation, the strain gradients on the surface of the stent bow become sharp and the interfaces between the coating and the stent have higher shear stress, which will accelerate the damaging of cohesive elements and result in the coating delamination. Furthermore, the local stress concentration of the coating leads to more micro-cracks in the deformed area, which is a potential problem for the application of the biodegradable magnesium alloy stents. Compared with the distinction between the two magnesium alloys AZ31 and JDBM, the design of stent plays a prominent role in the deformation. The distributions of Max. Principal Stress and PEEQ display completely different patterns between OPT and SIN stents (Fig.7j and 7k). Due to the design of the salient contour, the external deformation in the OPT stent is spread out to the two shoulders from the center area. The gradient width strut contour scattered the deformation center to the opposite sides (Fig.7k & 7l). The percentage of high plastic deformation of OPT stent is 4.36% (Fig. 8b). The numbers confirm that the high plastic deformation section of the stent decreases sharply when the deformation concentrated area is dispersed to both sides. The plastic deformation in the concentration was evenly distributed to vast areas, resulting the strain gradient on the stent surface become gentleness, which provides more favorable conditions for the adhesion of the coating.

The influence of polymer coating is also important to control the coating delamination. The analysis of the thickness and type of polymer coating is concurrent with the previous 2D result[28, 30], i.e.the thicker the coating, the higher the elastic modulus and yield strength of the coating, the more unfavorable the adhesion of the polymer coating on the surface of the stent. The stent design that well matches coating properties can help improve the clinical outcome of biodegradable Mg alloy stents.

This study has some limitations. First, the zero-thickness cohesive elements are sensitive to mass scaling in 3D modeling. In our work the target time increment is 2×10^{-6}s, a larger target time increment could lead to unstable degradation process of the cohesive elements, which means the computational time of 3D simulation is much higher than in a 2D space. Second, the balloon is simplified to a cylinder surface. The 3-fold balloon will lead to higher friction force on the coating surface, especially in the circumferential direction. Third, the property of the polymer coating is in dry conditions, considering that the validation experiment is carried out in vitro without liquid. When a stent is implanted the material property of PLGA and PLLA will change after immersion in blood and the interface strength between coating and stent will be reduced by hydration. Moreover the critical interface fracture energy $G_c{}'$ (Fig. 9) is an approximation value rather than a precise range, for reduce the amount of calculation.

CONCLUSIONS

This study provides an easily grasped and intelligible framework for understanding the deformation of both coating and stent struts, distinguishing the most important among the multiplying parameters, predicting delamination behavior, and providing guidelines for stent and coating designers.

The significant findings for the polymer coated biodegradable magnesium alloy cardiovascular stents are summarized as follows:

1) The debonding process started from luminal node extend to abluminal node, driven by the contact between balloon and coating.

2) JDBM with lower yield strength performed a more uniform strain and more favorable for adhesion of the coating, compared to the commercial magnesium alloy made of AZ31.
3) Shape optimization of stent improves the strain and stress distribution of coating observably, avoiding coating delamination.
4) PLGA coating with lower elastic modulus and yield strength, compared to PLLA polymer, tends to follow better the deformation of the stent and to adhere on the surface tightly.
5) A reduction in coating thickness and an increase in stent-coating interface strength improve the resistance to delamination.

Notes

The authors declare no competing financial interest.

ACKNOWLEDGEMENTS

This work was financially supported by the National Key Research and Development Program of China (2016YFC1102103), Science and Technology Commission of Shanghai Municipality (No.17XD1402100), the National Natural Science Foundation of China (No.51701041), the Committee of Shanghai Science and Technology (No.17DZ2200200) and Politecnico di Milano International Fellowships Program (PIF) .

REFERENCES

1. Stefanini , G. G.; Holmes , D. R. J., Drug-Eluting Coronary-Artery Stents. *New England Journal of Medicine* **2013,** *368* (3), 254-265.
2. Palmerini, T.; Benedetto, U.; Biondi-Zoccai, G.; Della Riva, D.; Bacchi-Reggiani, L.; Smits, P. C.; Vlachojannis, G. J.; Jensen, L. O.; Christiansen, E. H.; Berencsi, K.; Valgimigli, M.; Orlandi, C.; Petrou, M.; Rapezzi, C.; Stone, G. W., Long-Term Safety of Drug-Eluting and Bare-Metal Stents: Evidence From a Comprehensive Network Meta-Analysis. *Journal of the American College of Cardiology* **2015,** *65* (23), 2496-2507.
3. Im, S. H.; Jung, Y.; Kim, S. H., Current status and future direction of biodegradable metallic and polymeric

vascular scaffolds for next-generation stents. *Acta Biomaterialia* **2017,** *60*, 3-22.
4. Wykrzykowska, J. J.; Kraak, R. P.; Hofma, S. H.; van der Schaaf, R. J.; Arkenbout, E. K.; AJ, I. J.; Elias, J.; van Dongen, I. M.; Tijssen, R. Y. G.; Koch, K. T.; Baan, J., Jr.; Vis, M. M.; de Winter, R. J.; Piek, J. J.; Tijssen, J. G. P.; Henriques, J. P. S.; Investigators, A., Bioresorbable Scaffolds versus Metallic Stents in Routine PCI. *N Engl J Med* **2017,** *376* (24), 2319-2328.
5. Ali, Z. A.; Serruys, P. W.; Kimura, T.; Gao, R.; Ellis, S. G.; Kereiakes, D. J.; Onuma, Y.; Simonton, C.; Zhang, Z.; Stone, G. W., 2-year outcomes with the Absorb bioresorbable scaffold for treatment of coronary artery disease: a systematic review and meta-analysis of seven randomised trials with an individual patient data substudy. *The Lancet* **2017,** *390* (10096), 760-772.
6. Kereiakes, D. J.; Ellis, S. G.; Metzger, C.; Caputo, R. P.; Rizik, D. G.; Teirstein, P. S.; Litt, M. R.; Kini, A.; Kabour, A.; Marx, S. O.; Popma, J. J.; McGreevy, R.; Zhang, Z.; Simonton, C.; Stone, G. W., 3-Year Clinical Outcomes With Everolimus-Eluting Bioresorbable Coronary Scaffolds: The ABSORB III Trial. *Journal of the American College of Cardiology* **2017,** *70* (23), 2852-2862.
7. Wang, P.-J.; Ferralis, N.; Conway, C.; Grossman, J. C.; Edelman, E. R., Strain-induced accelerated asymmetric spatial degradation of polymeric vascular scaffolds. *Proceedings of the National Academy of Sciences* **2018,** *115* (11), 2640-2645.
8. Mao, L.; Shen, L.; Niu, J.; Zhang, J.; Ding, W.; Wu, Y.; Fan, R.; Yuan, G., Nanophasic biodegradation enhances the durability and biocompatibility of magnesium alloys for the next-generation vascular stents. *Nanoscale* **2013,** *5* (20), 9517-9522.
9. Zheng, Y. F.; Gu, X. N.; Witte, F., Biodegradable metals. *Materials Science and Engineering: R: Reports* **2014,** *77* (0), 1-34.
10. Esmaily, M.; Svensson, J. E.; Fajardo, S.; Birbilis, N.; Frankel, G. S.; Virtanen, S.; Arrabal, R.; Thomas, S.; Johansson, L. G., Fundamentals and Advances in Magnesium Alloy Corrosion. *Progress in Materials Science* **2017,** *89*, 92-193.
11. Haude, M.; Erbel, R.; Erne, P.; Verheye, S.; Degen, H.; Böse, D.; Vermeersch, P.; Wijnbergen, I.; Weissman, N.; Prati, F.; Waksman, R.; Koolen, J., Safety and performance of the drug-eluting absorbable metal scaffold (DREAMS) in patients with de-novo coronary lesions: 12 month results of the prospective, multicentre, first-in-man BIOSOLVE-I trial. *The Lancet* **2013,** *381* (9869), 836-844.
12. Haude, M.; Ince, H.; Abizaid, A.; Toelg, R.; Lemos, P. A.; von Birgelen, C.; Christiansen, E. H.; Wijns, W.; Neumann, F.-J.; Kaiser, C.; Eeckhout, E.; Lim, S. T.; Escaned, J.; Garcia-Garcia, H. M.; Waksman, R., Safety and performance of the second-generation drug-eluting absorbable metal scaffold in patients with de-novo coronary artery lesions (BIOSOLVE-II): 6 month results of a prospective, multicentre, non-randomised, first-in-man trial. *The Lancet* **2016,** *387* (10013), 31-39.
13. Jiang, W.; Tian, Q.; Vuong, T.; Shashaty, M.; Gopez, C.; Sanders, T.; Liu, H., Comparison Study on Four Biodegradable Polymer Coatings for Controlling Magnesium Degradation and Human Endothelial Cell Adhesion and Spreading. *ACS Biomaterials Science & Engineering* **2017,** *3* (6), 936-950.
14. Liu, J.; Zheng, B.; Wang, P.; Wang, X.; Zhang, B.; Shi, Q.; Xi, T.; Chen, M.; Guan, S., Enhanced in Vitro and in Vivo Performance of Mg–Zn–Y–Nd Alloy Achieved with APTES Pretreatment for Drug-Eluting Vascular Stent Application. *ACS Applied Materials & Interfaces* **2016,** *8* (28), 17842-17858.
15. Shi, Y.; Pei, J.; Zhang, L.; Lee, B. K.; Yun, Y.; Zhang, J.; Li, Z.; Gu, S.; Park, K.; Yuan, G., Understanding the effect of magnesium degradation on drug release and anti-proliferation on smooth muscle cells for magnesium-based drug eluting stents. *Corrosion Science* **2017,** *123*, 297-309.

16. Shi, Y.; Zhang, L.; Chen, J.; Zhang, J.; Yuan, F.; Shen, L.; Chen, C.; Pei, J.; Li, Z.; Tan, J.; Yuan, G., In vitro and in vivo degradation of rapamycin-eluting Mg-Nd-Zn-Zr alloy stents in porcine coronary arteries. *Materials Science and Engineering: C* **2017,** *80*, 1-6.

17. Ng, J.; Foin, N.; Ang, H. Y.; Fam, J. M.; Sen, S.; Nijjer, S.; Petraco, R.; Di Mario, C.; Davies, J.; Wong, P., Over-expansion capacity and stent design model: An update with contemporary DES platforms. *Int J Cardiol* **2016,** *221*, 171-9.

18. Watanabe, T.; Fujita, M.; Awata, M.; Iida, O.; Okamoto, S.; Ishihara, T.; Uematsu, M., Integrity of stent polymer layer after drug-eluting stent implantation: in vivo comparison of sirolimus-, paclitaxel-, zotarolimus- and everolimus-eluting stents. *Cardiovascular Intervention and Therapeutics* **2014,** *29* (1), 4-10.

19. Levy, Y.; Mandler, D.; Weinberger, J.; Domb, A. J., Evaluation of drug-eluting stents' coating durability—Clinical and regulatory implications. *Journal of Biomedical Materials Research Part B: Applied Biomaterials* **2009,** *91B* (1), 441-451.

20. Karanasiou, G. S.; Papafaklis, M. I.; Conway, C.; Michalis, L. K.; Tzafriri, R.; Edelman, E. R.; Fotiadis, D. I., Stents: Biomechanics, Biomaterials, and Insights from Computational Modeling. *Annals of Biomedical Engineering* **2017,** *45* (4), 853-872.

21. McHugh, P.; Barakat, A.; McGinty, S., Medical Stents: State of the Art and Future Directions. *Annals of Biomedical Engineering* **2015,** *44* (2), 274-275.

22. Bressloff, N. W.; Ragkousis, G.; Curzen, N., Design Optimisation of Coronary Artery Stent Systems. *Annals of biomedical engineering* **2015**, 1-11.

23. Grogan, J. A.; Leen, S. B.; McHugh, P. E., Optimizing the design of a bioabsorbable metal stent using computer simulation methods. *Biomaterials* **2013**.

24. Wu, W.; Petrini, L.; Gastaldi, D.; Villa, T.; Vedani, M.; Lesma, E.; Previtali, B.; Migliavacca, F., Finite Element Shape Optimization for Biodegradable Magnesium Alloy Stents. *Annals of Biomedical Engineering* **2010,** *38* (9), 2829-2840.

25. Wu, W.; Chen, S.; Gastaldi, D.; Petrini, L.; Mantovani, D.; Yang, K.; Tan, L.; Migliavacca, F., Experimental data confirm numerical modeling of the degradation process of magnesium alloys stents. *Acta Biomaterialia* **2013,** *9* (10), 8730-8739.

26. Gu, Z.; Li, S.; Zhang, F.; Wang, S., Understanding Surface Adhesion in Nature: A Peeling Model. *Advanced Science* **2016,** *3* (7), 1500327-n/a.

27. Diehl, T., On using a penalty-based cohesive-zone finite element approach, Part I: Elastic solution benchmarks. *International Journal of Adhesion and Adhesives* **2008,** *28* (4–5), 237-255.

28. Hopkins, C. G.; McHugh, P. E.; McGarry, J. P., Computational Investigation of the Delamination of Polymer Coatings During Stent Deployment. *Annals of Biomedical Engineering* **2010,** *38* (7), 2263-2273.

29. Hopkins, C.; McHugh, P. E.; O'Dowd, N. P.; Rochev, Y.; McGarry, J. P., A combined computational and experimental methodology to determine the adhesion properties of stent polymer coatings. *Computational Materials Science* **2013,** *80*, 104-112.

30. Hopkins, C.; Sweeney, C. A.; O'Connor, C.; McHugh, P. E.; McGarry, J. P., Webbing and Delamination of Drug Eluting Stent Coatings. *Annals of Biomedical Engineering* **2015,** *44* (2), 1-13.

31. WU, W.; MERCURI, M.; PEDRONI, C.; MIGLIAVACCA, F.; PETRINI, L., A COMPUTATIONAL STUDY TO INVESTIGATE DEBONDING IN COATED BIORESORBABLE STENTS. *Journal of Mechanics in Medicine and Biology* **2015,** *15* (02), 1540015.

32. Zhang, J.; Kong, N.; Shi, Y.; Niu, J.; Mao, L.; Li, H.; Xiong, M.; Yuan, G., Influence of proteins and cells on in vitro

corrosion of Mg–Nd–Zn–Zr alloy. *Corrosion Science* **2014,** *85* (0), 477-481.

33. Liu, F.; Chen, C.; Niu, J.; Pei, J.; Zhang, H.; Huang, H.; Yuan, G., The processing of Mg alloy micro-tubes for biodegradable vascular stents. *Materials Science and Engineering: C* **2015,** *48*, 400-407.

34. Zhang, J.; Li, H.; Wang, W.; Huang, H.; Pei, J.; Qu, H.; Yuan, G.; Li, Y., The degradation and transport mechanism of a Mg-Nd-Zn-Zr stent in rabbit common carotid artery: A 20-month study. *Acta Biomaterialia* **2018,** *69*, 372-384.

35. Paryab, N.; Cronin, D.; Lee-Sullivan, P.; Ying, X.; Boey, F. Y.; Venkatraman, S., Uniform expansion of a polymeric helical stent. *Journal of Medical Devices* **2012,** *6* (2), 021012.

36. De Falco, P.; Barbieri, E.; Pugno, N.; Gupta, H. S., Staggered Fibrils and Damageable Interfaces Lead Concurrently and Independently to Hysteretic Energy Absorption and Inhomogeneous Strain Fields in Cyclically Loaded Antler Bone. *ACS Biomaterials Science & Engineering* **2017,** *3* (11), 2779-2787.

37. Wei, W.; Petrini, L.; Altomare, L.; Farè, S.; Tremamunno, R.; Zhentao, Y.; Migliavacca, F., Modeling and Experimental Studies of Peeling of Polymer Coating for Biodegradable Magnesium Alloy Stents. *Rare Metal Materials and Engineering* **2014,** *43* (12), 2877-2882.

38. Lucchini, R.; Cattarinuzzi, E.; Maraghechi, S.; Gastaldi, D.; Adami, A.; Lorenzelli, L.; Vena, P., Delamination phenomena in aluminum/polyimide deformable interconnects: In-situ micro-tensile testing. *Materials & Design* **2016,** *89*, 121-128.

39. Gu, X.; Mao, Z.; Ye, S.-H.; Koo, Y.; Yun, Y.; Tiasha, T. R.; Shanov, V.; Wagner, W. R., Biodegradable, elastomeric coatings with controlled anti-proliferative agent release for magnesium-based cardiovascular stents. *Colloids and Surfaces B: Biointerfaces* **2016,** *144*, 170-179.